**Research Article**

# Construction and performance of CdS/MoO₂@Mo₂C-MXene photocatalyst for H₂ production

Sen JIN, Huijuan JING, Libo WANG, Qianku HU, Aiguo ZHOU[*]

*School of Materials Science and Engineering, Henan Polytechnic University, Jiaozuo 454003, China*

**Abstract:** Nowadays, photocatalytic technologies are regarded as promising strategies to solve energy problems, and various photocatalysts have been synthesized and explored. In this paper, a novel CdS/MoO₂@Mo₂C-MXene photocatalyst for H₂ production was constructed by a two-step hydrothermal method, where MoO₂@Mo₂C-MXene acted as a binary co-catalyst. In the first hydrothermal step, MoO₂ crystals with an egged shape grew on the surface of two-dimensional (2D) Mo₂C MXene via an oxidation process in HCl aqueous solution. In the second hydrothermal step, CdS nanorods were uniformly assembled on the surface of MoO₂@Mo₂C-MXene in ethylenediamine with an inorganic cadmium source and organic sulfur source. The CdS/MoO₂@Mo₂C-MXene composite with MoO₂@Mo₂C-MXene of 5 wt% exhibits an ultrahigh visible-light photocatalytic H₂ production activity of 22,672 μmol/(g·h), which is ~21% higher than that of CdS/Mo₂C-MXene. In the CdS/MoO₂@Mo₂C-MXene composite, the MoO₂ with metallic nature separates CdS and Mo₂C MXene, which acts as an electron-transport bridge between CdS and Mo₂C MXene to accelerate the photoinduced electron transferring. Moreover, the energy band structure of CdS was changed by MoO₂@Mo₂C-MXene to suppress the recombination of photogenerated carriers. This novel compound delivers upgraded photocatalytic H₂ evolution performance and a new pathway of preparing the low-cost photocatalyst to solve energy problems in the future.

**Keywords:** Mo₂C MXene; MoO₂; CdS; photocatalysis; H₂ production

## 1 Introduction

H₂ is a clean, eco-friendly, and pollution-free gas, which is considered as promising energy. Semiconductor photocatalysis is a convenient and low-cost approach of continuously obtaining H₂. Owing to the narrow bandgap, appropriate conduction band position, and good electronic charge transfer capability [1,2], CdS has been proved to be one of the most prominent semiconductor photocatalysts for H₂ production. However, the rapid recombination rate of the photoinduced electron–hole pairs restricts the performance of CdS [3,4]. Coupling CdS with other materials to form heterojunctions can effectively separate the photogenerated electron–hole pairs by electron trapping and proper band alignment. Noble metals, such as Pt, Au, Pd, etc. [5,6], have been deposited onto CdS to construct hybridized systems as co-catalysts, and accelerate reaction kinetics by facilitating the transfer of charge carriers and their spatial separation. Nonetheless, the limitation of high price, extreme scarcity, and complicated synthetic processes affect the

* Corresponding author.

E-mail: zhouag@hpu.edu.cn

commercialization of current photocatalysts with the noble metals. Therefore, it is significant to develop high-performance CdS-based photocatalysts by coupling with low-cost materials, such as the transition metal sulfide [7–10], transition metal oxide [11,12], graphene oxide [13], hydroxide [14], carbide [15], etc.

MXenes are a series of two-dimensional (2D) transition metal carbides, nitrides, or carbonitrides with a general formula of $M_{n+1}X_nT_x$ ($n$ = 1, 2, and 3), where M is an early transition metal, X is a carbon or nitrogen, and $T_x$ stands for various surface terminations (–OH, –O, and –F). Normally, MXenes are prepared by etching A element from the MAX phase [16–20] and have shown great potential in various fields due to the numerous hydrophilic functionalities on the surface of MXenes, excellent metallic conductivity, and exposed terminal transition metal sites [21–24]. Theoretically, MXenes have been predicted as promising photocatalysts for water splitting in 2016 [25]. Subsequently, numerous research confirmed that MXene-based co-catalysts are promising candidates for the $H_2$ production [26–37]. Notably, among these works, only $Ti_3C_2$ MXene, the first member of MXenes, was considered, though there are many MXenes with different compositions. $Mo_2C$ MXene is another MXene prepared by etching $Mo_2Ga_2C$ [38–42]. In the previous work [43], we found that $Mo_2C$-MXene/CdS heterostructure exhibited an ultra-high $H_2$ production rate of 17,964 μmol/(g·h).

Although the photocatalytic performance of $Mo_2C$ MXene as the co-catalyst is superior to most other MXenes, the photocatalytic activity tends to decrease within the irradiation time. This is because that MXenes are not stable during the irradiation. To increase the stability, $Mo_2C$ MXene needs to be partly covered by a stable layer. Moreover, the layer needs to be very thin with high electrical conductivity and potential for faster charge-carrier transfer between MXene and CdS. Therefore, if a thin layer with high stability and high conductivity is introduced at the MXene–CdS interface, the deterioration tendency of the catalyst can be improved because of the high stability, and the catalytic performance can be improved due to the faster charge-carrier transferring.

$MoO_2$ is a metallic oxide with high stability and high electrical conductivity. It can be *in-situ* generated from the oxidation of $Mo_2C$ MXene. Therefore, the $MoO_2$ thin layer can be introduced at the interface between $Mo_2C$ MXene and CdS to enhance and stabilize the photocatalytic activity. In view of this, a novel catalyst with the structure of $CdS/MoO_2@Mo_2C$ was designed in this paper. The catalyst showed higher and more stable catalytic performance compared to $CdS/Mo_2C$. In the catalyst, $MoO_2$ and $Mo_2C$ MXene act as dual co-catalysts to increase the catalytic activity of CdS.

To construct the novel dual co-catalyst system, $Mo_2C$ MXene was oxidized and covered by the *in-situ* generated $MoO_2$ to obtain $MoO_2@Mo_2C$-MXene structure. Then the CdS nanocrystals are assembled with the $MoO_2@Mo_2C$-MXene. A two-step hydrothermal method was used to make the catalyst. In the first step, the $MoO_2$ nanoparticles *in-situ* grew on the surface of $Mo_2C$ MXene sheets to form $MoO_2@Mo_2C$-MXene hybrid via an oxidation process in HCl aqueous solution. Subsequently, in the second step, in the ethylenediamine with an inorganic cadmium source ($Cd(NO_3)_2·4H_2O$) and an organic sulfur source (thiourea), $Cd^{2+}$ and $S^{2-}$ were self-assembled on the surface of $MoO_2@Mo_2C$-MXene to form a heterostructure of $CdS/MoO_2@Mo_2C$. The heterostructure indeed possessed better photophysical and photoelectrochemical properties compared to $CdS/Mo_2C$, and exhibited an ultra-high photocatalytic activity.

## 2 Experimental

### 2. 1 Synthesis of Mo₂C MXene

Highly pure $Mo_2C$ MXene was made by a hydrothermal strategy [44]. Briefly, $Mo_2Ga_2C$ powders (lab-made) of 1 g [39–41] were mixed with HF (40%) solution of 40 mL and sealed in a Teflon-lined autoclave. The autoclave was ultrasonically treated for 30 min and kept at 160 ℃ for 24 h. Then the black sediments in the solution were washed with de-ionized water and ethanol until pH = 6. Finally, the obtained powders were dried at 60 ℃ for 12 h in vacuum, which were $Mo_2C$ MXene powders.

### 2. 2 Synthesis of MoO₂@Mo₂C-MXene composite

$NaBF_4$ (99.9%, Macklin, China) of 0.2 g, as the directing reagent, was dissolved in 1.0 M HCl solution of 15 mL (36–38 wt%, Yantai Shuangshuang Chemical, China) and stirred for 30 min. $Mo_2C$ MXene powders of 0.1 g were added into the above mixed solution, and the solution was stirred for 30 min, followed by ultrasonication for 30 min. The suspension was sealed

in a Teflon-lined autoclave and hydrothermally treated at 180 ℃ for 24 h. Thereafter, the powders of $MoO_2@Mo_2C$-MXene composite were collected, which were washed with the de-ionized water and ethanol until neutral and dried at 60 ℃ for 12 h in vacuum.

## 2. 3 Assembly of CdS with $MoO_2@Mo_2C$-MXene

$Cd(NO_3)_2 \cdot 4H_2O$ (analytical reagent (AR) 99%, Macklin, China) of 1.53 g and thiourea (AR 99%, Shanghai Aladdin Biochemical Technology, China) of 1.14 g, as the precursors of CdS, were dissolved in the de-ionized water of 40 mL and stirred for 30 min. A certain amount of $MoO_2@Mo_2C$-MXene powders were dispersed in the solution and strongly ultrasonic treated for 1 h. Thereafter, the ethylenediamine (AR 99%, Luoyang Chemical Reagent Factory, China) of 10 mL was added into the above solution and stirred for another 30 min. Then the mixed solution was sealed in a Teflon-lined autoclave and kept at 180 ℃ for 24 h to synthesize $CdS/MoO_2@Mo_2C$ by a solvothermal process. The final precipitates with golden color were separated from the solution by centrifugalizing. The powders were washed with the de-ionized water and ethanol several times until neutral, and dried at 60 ℃ in vacuum for 12 h. According to the mass ratio of $MoO_2@Mo_2C$-MXene composite to CdS (0.1, 1, 2.5, 5, and 7 wt%), the prepared samples were labelled as CMM$x$ ($x$ = 0.1, 1, 2.5, 5, and 7). As reference samples, $CdS/Mo_2C$ and $CdS/MoO_2$ with the optimal loading of co-catalyst ($Mo_2C$ MXene of 2.5 wt% for $CdS/Mo_2C$ and $MoO_2$ of 5 wt% for $CdS/MoO_2$) were made through the identical preparation process.

## 2. 4 Materials characterizations

All the samples were tested by X-ray diffraction (XRD, Smart-lab, Rigaku Corporation, Japan) by using Cu Kα ($\lambda$ = 1.5406 Å) radiation, observed by a scanning electron microscope (SEM, Merlin Compact, Zeiss, Germany) equipped with an energy disperse spectroscope (EDS, X-MaxN, Oxford Instruments, UK) and a transmission electron microscope (TEM, JEM-2100F, JEOL, Japan) with an accelerating voltage of 200 kV. The chemical components of the products were characterized by an X-ray photoelectron spectrometer (XPS, ESCALAB 250X, Thermo Fischer Scientific, USA) with an Al Kα source ($hv$ = 1486.6 eV) of 12.5 kV. The Brunauer–Emmett–Teller specific surface area ($S_{BET}$) was measured by $N_2$ adsorption at 77 K

using an adsorption analyzer (ASAP2460, Micromeritics Instruments, USA). The ultraviolet–visible (UV–Vis) diffuse reflectance spectra (DRS) were tested by dry-pressing disk samples with an ultraviolet–visible spectrophotometer (UH4150, Hitachi, Japan) and using $BaSO_4$ as the reflectance standard. The photoluminescence (PL) spectra were evaluated by a spectrofluorophotometer (Fluoromax-4, Horiba, Japan) under the excitation of 350 nm at room temperature.

## 2. 5 Photocatalytic $H_2$-production measurements

The photocatalytic experiments were tested by a photocatalytic activity evaluation system (CEL-SPH2N, Beijing China Education Au-light Technology, China). A quartz vessel of 250 mL was used to carry out the water-splitting reaction. The quartz vessel was maintained at room temperature and vacuumed until the pressure was maintained at −0.1 MPa during the reaction. A Xe lamp of 300 W equipped with a cut-off filter ($\lambda \geqslant$ 420 nm) was utilized as the light source (ca. 80 mW/cm$^2$ for the focused intensity on the sample in the mixed solution). The photocatalyst of 20 mg was added into the aqueous solution of 50 mL containing the lactic acid (AR 85%) of 10 mL as the sacrificial reagent solution and the de-ionized water of 40 mL with stirring continuously in the range of 15–20 ℃. The generated $H_2$ during irradiation was analyzed by a gas chromatograph (TCD, TDX01 column, CEL-GC7920, Beijing China Education Au-light Technology, China) with $N_2$ as a carrier gas. The apparent quantum efficiency (AQE) was measured under the identical photocatalytic conditions except for the replacement of the Xe lamp with a monochromatic cut-off filter ($\lambda$ = 420 nm) as the light source to trigger the photocatalytic reaction. The focused intensity for 420 nm irradiation was ca. 6 mW/cm$^2$.

## 2. 6 Electrochemical and photoelectrochemical measurements

The photoelectrochemical measurements were conducted on an electrochemical analyzer (CHI760E, Chenhua Instruments, China) in a standard three-electrode system by using the samples as the working electrodes, Ag/AgCl as the reference electrode, and the Pt wire as the counter electrode. The transient photocurrent (TPC) measurements were carried out under the visible light irradiation ($\lambda \geqslant$ 420 nm) with on/off switches at a bias of 0.2 V (vs. Ag/AgCl). The electrochemical

impedance spectra (EIS) experiments were performed at a bias of 0.9 V (vs. Ag/AgCl) under the visible light irradiation ($\lambda \geqslant 420$ nm). The Mott–Schottky plots were recorded over the AC frequency of 1000 Hz in the dark. The electrolytes in all the electrochemical measurements were 0.5 M $Na_2SO_4$ aqueous solution. The working electrodes were synthesized as follows: the as-prepared samples of 10 mg were dispersed in the mixed aqueous solution containing the de-ionized water of 375 μL, the ethanol of 125 μL, and the Nafion of 50 μL by ultrasonication for 2 h to make uniform slurry. Thereafter, the slurry was coated onto a fluorine doped tin oxide (FTO) glass plate of 10 mm × 25 mm, and the obtained electrodes were dried in air for 24 h.

## 3   Results and discussion

### 3. 1   Synthesis and characterization of CdS/MoO₂@Mo₂C

The XRD patterns of as-prepared samples were shown in Fig. 1. The standard patterns of $MoO_2$ (PDF Card No. 78-1069) and wurtzite CdS (PDF Card No. 77-2306) are also shown in the figure. $Mo_2Ga_2C$ is a new compound found in 2015 [38]. The standard pattern of $Mo_2Ga_2C$ reported in Ref. [38] is shown in the figure. As shown in Fig. 1, the $Mo_2Ga_2C$ powders made in this paper for starting material are highly pure $Mo_2Ga_2C$ [41]. After etching, the powders converted to $Mo_2C$ MXene with the feature of the strong characteristic peak of (002) that shifts to a low angle [43,44]. From the comparison of the two patterns, $Mo_2C$ MXene was successfully made from $Mo_2Ga_2C$. The top pattern in Fig. 1(a) is the pattern of $Mo_2C$ MXene oxidized by the hydrothermal process ($MoO_2$@$Mo_2C$-MXene). Compared with the XRD patterns of $Mo_2C$ MXene and standard $MoO_2$, the emergence of $MoO_2$ is evidenced by the obvious diffraction peaks of $MoO_2$ (PDF Card No. 78-1069). The co-existence of $Mo_2C$ MXene and $MoO_2$ indicates the successful synthesis of the $MoO_2$@$Mo_2C$-MXene composite.

The XRD patterns of CdS assembled with different amounts of $MoO_2$@$Mo_2C$-MXene, named as CMM*x* (*x* = 0.1, 1, 2.5, 5, and 7), are shown in Fig. 1(b). Compared with the standard wurtzite CdS shown in the bottom of Fig. 1(b), all patterns correspond well with the wurtzite phase (PDF Card No. 77-2306). Thus, CdS with the wurtzite crystal structure was obtained by this method. In general, CdS has two crystal structures:
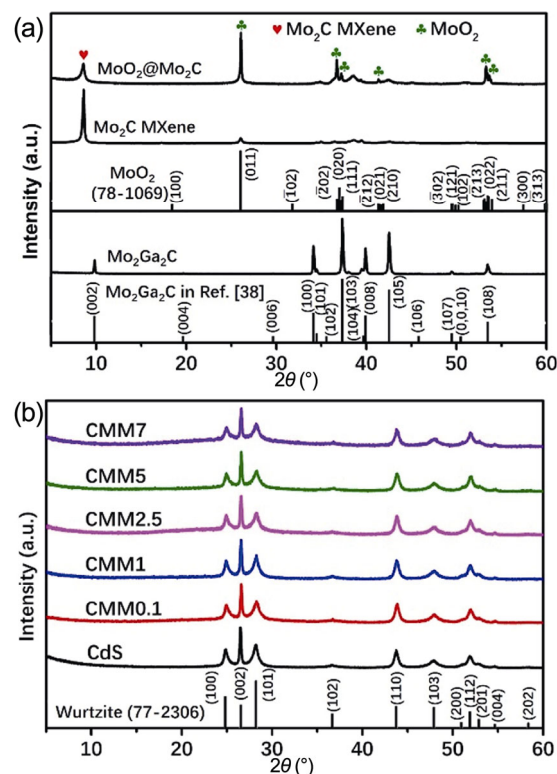


**Fig. 1** XRD patterns of (a) $Mo_2Ga_2C$, $Mo_2C$ MXene, and $MoO_2$@$Mo_2C$-MXene composite and (b) CMM*x* samples and the corresponding standard patterns.

wurtzite (high-temperature phase) and sphalerite (low-temperature phase). Normally, the wurtzite CdS, the phase obtained in this work, has better photocatalytic performance compared to the sphalerite CdS [45].

The microstructure images of as-prepared samples are shown in Fig. 2. As shown in Fig. 2(a), the microstructure of $Mo_2C$ MXene is 2D flakes, similar to its precursor $Mo_2Ga_2C$ [39–41]. From Fig. 2(b), for $MoO_2$@$Mo_2C$-MXene sample, egg-shaped $MoO_2$ crystals appear on the surface of $Mo_2C$ MXene flakes, which grew during the hydrothermal oxidation with the assistance of $NaBF_4$ as the directing reagent. As shown in Fig. 2(c), the CdS/$MoO_2$@$Mo_2C$ sample exhibits an acanthosphere structure that consists of the rod-like CdS crystals. Besides, a bare 2D $Mo_2C$ MXene sheet was observed among several acanthospheres in Fig. S1(a) in the Electronic Supplementary Material (ESM), which is marked by a red cycle. In the corresponding high magnification image (Fig. S1(b) in the ESM), a few immature CdS particles appear on the surface of $Mo_2C$ MXene, illustrating how the CdS nanorods grew up at the beginning of the hydrothermal reaction.

It is worth noting that, the hydrothermal oxidation not only facilitated the growth of $MoO_2$ on $Mo_2C$
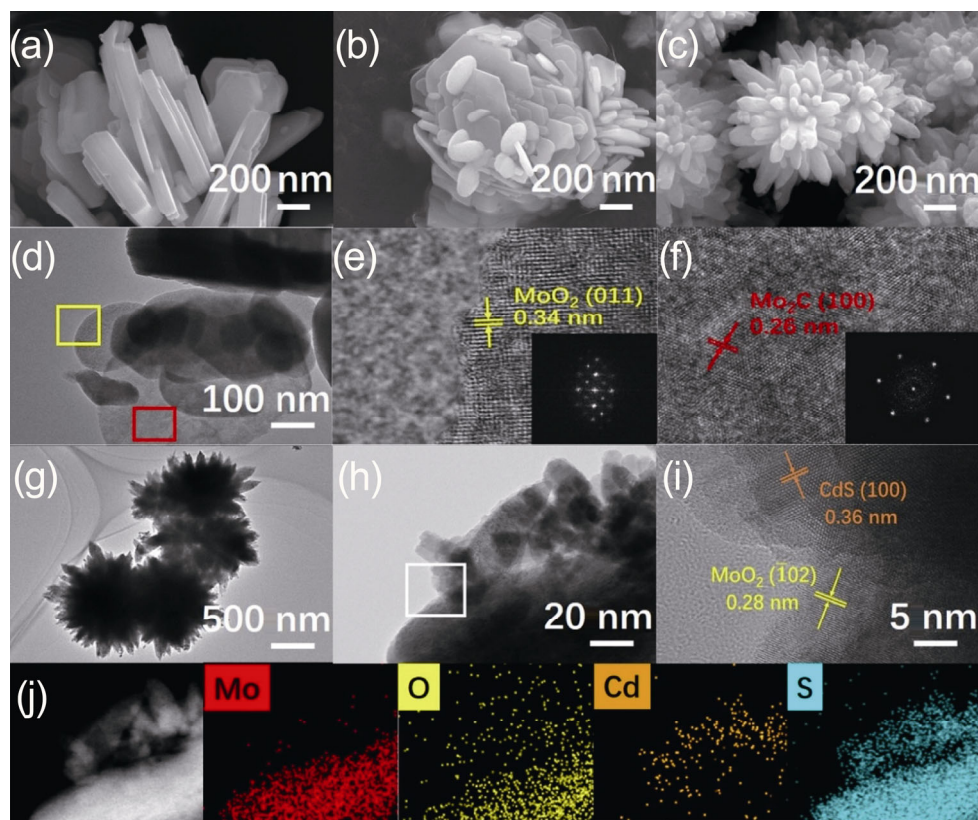
**Fig. 2** (a–c) SEM images of Mo$_2$C MXene, MoO$_2$@Mo$_2$C-MXene, and CdS/MoO$_2$@Mo$_2$C samples, respectively. (d) TEM image of MoO$_2$@Mo$_2$C-MXene after ultrasonic treatment. (e, f) High-resolution TEM images of MoO$_2$@Mo$_2$C-MXene corresponding to the region of yellow and red rectangles in (d), respectively (insets: the electron diffraction patterns). (g) TEM image of CdS/MoO$_2$@Mo$_2$C. (h) High magnification TEM image of CdS/MoO$_2$@Mo$_2$C after breaking the particles. (i) Close observation to the area highlighted by the rectangle region in (h). (j) STEM image and the corresponding elemental mappings.

MXene, but also made Mo$_2$C MXene flakes more transparent to electrons in the SEM observation. Figure S2(a) in the ESM shows that some loose Mo$_2$C MXene sheets in the red block diagram exhibit the transparent feature of electrons. The high magnification SEM image (Fig. S2(b) in the ESM) shows that the below flakes can be observed due to the electron transparency of Mo$_2$C MXene sheets. Besides, abundant cracks, which are similar to defects, are observed clearly on the 2D sheets. On the contrary, the Mo$_2$C MXene before the hydrothermal oxidation shows a smooth layered morphology without obvious cracks (Fig. S2(c) in the ESM). According to the previous research, the defects and nanopores in the Mo$_2$C MXene flakes are beneficial to the energy storage or catalysis [46].

The TEM image of MoO$_2$@Mo$_2$C-MXene is shown in Fig. 2(d). Many 2D crystals with the typical MXene structure were observed (marked by a red rectangle), and a crystal with an egg shape was observed (marked by a yellow rectangle). The high-resolution TEM (HRTEM) image of the yellow rectangle is shown in

Fig. 2(e). The lattice plane with *d* spacing of 0.34 nm is attributed to the (011) plane of MoO$_2$. The electron diffraction pattern in the inset of Fig. 2(e) confirms that it is a monoclinic phase of MoO$_2$ with the P2$_1$/c space group [47]. The HRTEM image of the red rectangle is shown in Fig. 2(f). The *d*-spacing estimated in Fig. 2(f) is 0.26 nm, corresponding to the (100) planes of Mo$_2$C MXene. The electron diffraction pattern in the inset of Fig. 2(f) shows that it is the hexagonal crystal of Mo$_2$C MXene. Based on the above analysis, the two type crystals in Fig. 2(d) correspond to the MoO$_2$ and Mo$_2$C MXene. As shown in Fig. S3 in the ESM, the MoO$_2$ crystal with the egg shape was derived from Mo$_2$C MXene and gradually grew up until the Mo$_2$C MXene sheets were completely covered.

The TEM image of CdS/MoO$_2$@Mo$_2$C with an acanthosphere shape is shown in Fig. 2(g). To observe the core of the acanthosphere, the sample was further treated by ultrasound for breaking the particles. The TEM image is shown in Fig. S4 in the ESM, which reveals that the CdS nanorods with a radial arrangement

grew on the core of MoO$_2$@Mo$_2$C-MXene composite. A high magnification TEM image in Fig. 2(h) shows the formed heterostructures between CdS and MoO$_2$@Mo$_2$C-MXene composite. The lattice fringes of 0.36 nm of the nanoparticle observed by the HRTEM in Fig. 2(i) are attributed to the (100) facets of hexagonal wurtzite CdS, which further indicates that the CdS nanorods synthesized in this work are the dominant wurtzite phase. Besides, the lattice fringes of 0.28 nm agree well with the ($\bar{1}$02) facets of MoO$_2$. The scanning transmission electron microscopy (STEM) image (Fig. 2(j)) and the corresponding element mappings focusing on the heterostructures clearly identify the component distribution. Mo and O are mainly distributed in the bottom crystal in Fig. 2(j), corresponding to MoO$_2$. The distribution of Cd and S in the top crystal confirms the existence of CdS.

The chemical composition and bonding states of CMM5 were tested by an X-ray photoelectron spectrometer (XPS). The XPS survey spectrum is shown in Fig. S5 in the ESM, which displays that Cd, O, C, Mo, and S are dominant elements. Figure 3(a) shows the XPS spectra in the Mo 3d region before and after the combination of MoO$_2$@Mo$_2$C-MXene and CdS. The Mo 3d spectrum of MoO$_2$@Mo$_2$C-MXene can be divided into two main peaks, as clearly shown in Fig. 3(a). The peaks centered at 229.6 and 232.8 eV can be ascribed to the Mo–C species in Mo$_2$C MXene [46]. Significantly, the binding energy of Mo–C species at 229.6 eV is 1.5 eV higher than that of the Mo–C species (228.1 eV) in Mo$_2$Ga$_2$C [48], indicating the replacement of the Ga element by plenty of electronegative surface functional groups (O, OH, and/or F) during the etching process [49]. The binding energy peaks of Mo 3d$_{5/2}$ (230.0 eV) and Mo 3d$_{3/2}$ (233.1 eV) components are characteristics of Mo$^{4+}$ [50], i.e., MoO$_2$ derived from Mo$_2$C MXene, while the other two weaker peaks at 231.2 and 235.6 eV correspond to Mo$^{5+}$ or Mo$^{6+}$ [48,51], suggesting that a small number of other forms of molybdenum oxide, such as MoO$_3$, co-exist in the generated MoO$_2$ during the hydrothermal treatment. For the CMM5 sample, a strong peak at 225.45 eV appears in the Mo 3d experimental signal, which is intensively associated with the formation of Mo–S bonds [52].

The XPS spectra in S 2p and Cd 3d are shown in Figs. 3(b) and 3(c), respectively. Compared with the pure CdS, the peaks of S 2p and Cd 3d in the CMM5 sample both shift towards a higher binding energy direction, owing to the decreased electronic density of Cd and S after coupling with MoO$_2$@Mo$_2$C-MXene and the formed heterojunction interaction [53].

The N$_2$ adsorption–desorption isotherms and the pore size distributions are shown in Fig. S6 in the ESM. All the samples exhibit similar type IV isotherms with a well-defined H3 hysteresis loop (Fig. S6(a) in the ESM), demonstrating the presence of mesopores [54]. According to Barrett–Joyner–Halenda method, the calculated distribution curves of CMM$x$ samples are shown in Fig. S6(b) in the ESM. The pore sizes of all samples are mainly in the range of 4–30 nm (mesopores), while a small number of pores have a size above 50 nm, even 100 nm (macropores). The presence of such a hybrid pore size of mesopores and macropores is beneficial to the contact between the reactant and the photocatalyst and facilitates the photocatalytic process [55]. The $S_{BET}$ of all the CdS/MoO$_2$@Mo$_2$C is shown in Table S1 in the ESM. The results reveal that all the samples have similar $S_{BET}$ from 14.3 to 15.5 m$^2$/g.

According to the experimental results and discussion above, the typical synthesis route of CdS/MoO$_2$@Mo$_2$C nanoparticles is schematically depicted in Fig. 4. MoO$_2$ was formed on the surface of Mo$_2$C MXene due to oxidation with the help of HCl in the first hydrothermal
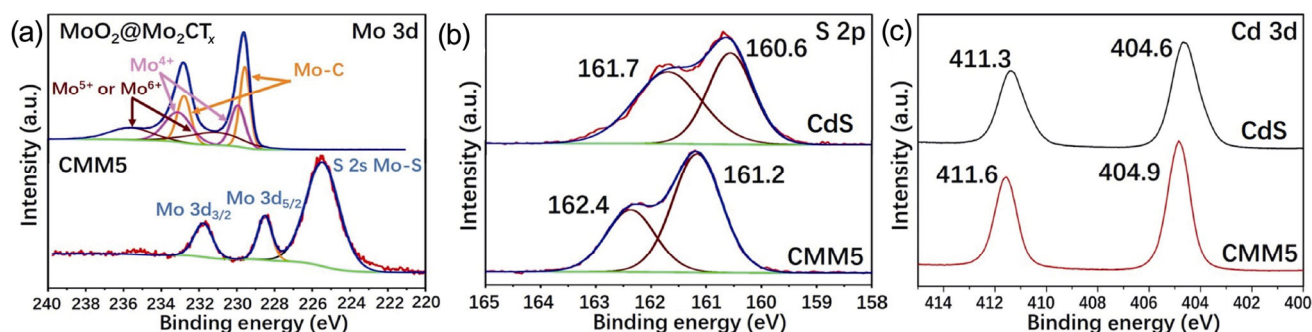


**Fig. 3**  (a) High resolution XPS spectra of MoO$_2$@Mo$_2$C-MXene and CMM5 in the Mo 3d region. High resolution XPS spectra of CdS and CMM5 in (b) S 2p region and (c) Cd 3d region.
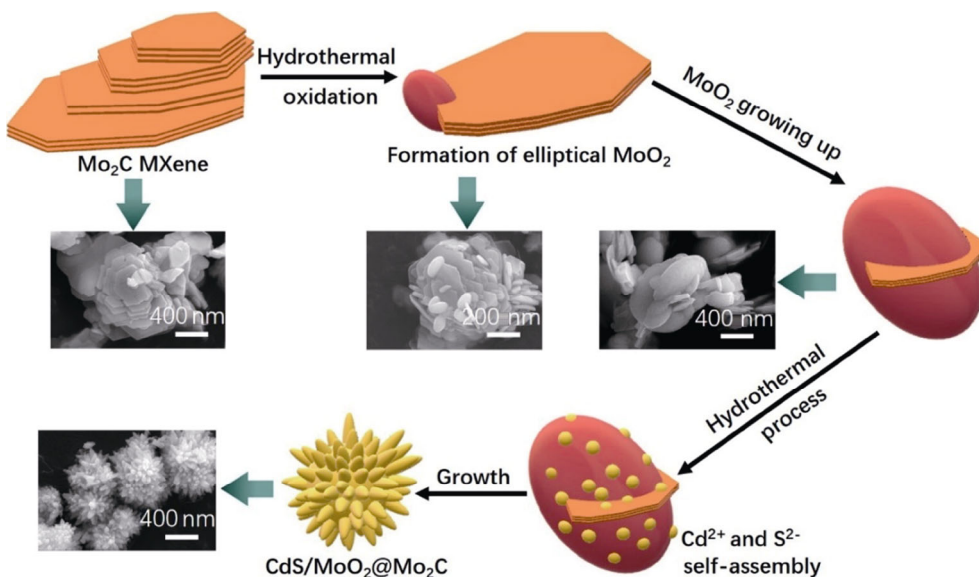
**Fig. 4**   Schematic illustration of the synthesis of $CdS/MoO_2@Mo_2C$ nanoparticles.

process. Thus, the $MoO_2@Mo_2C$-MXene composite was obtained. Then, the CdS nanocrystals nucleated and grew up on the surface of the $MoO_2@Mo_2C$-MXene composite in the second hydrothermal process. Finally, the $CdS/MoO_2@Mo_2C$ nanoparticles in the acanthosphere shape were obtained.

## 3. 2   Photocatalytic properties

The photocatalytic $H_2$ production of $CdS/MoO_2@Mo_2C$ samples (20 mg) was evaluated at room temperature under the visible light with the lactic acid as the sacrificial agent. The activities of each sample for the $H_2$ production (illumination for 4 h) are displayed in Fig. 5(a), and the $H_2$ production rates are shown in Fig. 5(b). The pure CdS sample presents a low $H_2$ production rate of 1923 μmol/(g·h) in Fig. 5(b), while the $H_2$ evolution performance is significantly boosted with the addition of $MoO_2@Mo_2C$-MXene for CMM$x$ ($x$ = 0.1, 1, 2.5, 5, and 7). The number of formed heterostructures

between CdS and $MoO_2@Mo_2C$-MXene increases with the loading of $MoO_2@Mo_2C$-MXene, which is beneficial to the enhancement of photocatalytic activity. In particular, the optimal sample of CMM5 exhibits the best $H_2$ production rate of 22,672 μmol/(g·h), which is ~21% higher than that of $CdS/Mo_2C$ [43]. The reduction of photocatalytic activity with the further increase of $MoO_2@Mo_2C$-MXene is probably because excessive $MoO_2@Mo_2C$-MXene can cover the active sites of the catalysts [28,56]. Furthermore, the photocatalytic activity of CMM5 was repeatedly observed under the same reaction conditions for the three recycling tests (Fig. 5(c)). High stability of photocatalytic activity for CMM5 was maintained during each cyclicity experiment, indicating the excellent photo-stability of heterostructure between CdS and $MoO_2@Mo_2C$-MXene.

The AQE of the samples was evaluated under the identical photocatalytic conditions except that a
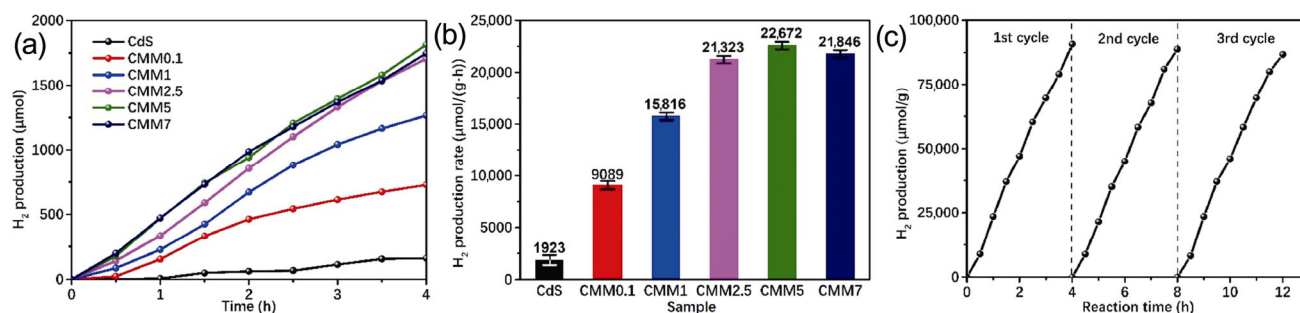


**Fig. 5**   (a) Plots of the integrated amounts of $H_2$ production versus the irradiation time of the samples of 20 mg under the visible light. (b) Rates of $H_2$ production of samples. (c) Cyclicity experiment of $H_2$ production performance of CMM5.

monochromatic light resource ($\lambda$ = 420 nm) was employed to trigger the photocatalytic reactions. As shown in Table S2 in the ESM, the results of AQE are in accordance with the photocatalytic $H_2$ production experiments that CMM5 can more effectively transform the absorbed photons into $H_2$ molecules (49.2%).

To further investigate the effect of the structure of $CdS/MoO_2@Mo_2C$ in the photocatalysis process, the photocatalysis of CdS coupled with only $MoO_2$ (99%, Shanghai Aladdin Biochemical Technology, China) or $Mo_2C$ MXene under the identical preparation technology was evaluated in the same photocatalytic measurements and compared with that of the CMM5 sample in Fig. S7(a) in the ESM. The $H_2$ production rates of optimal $CdS/MoO_2$ and $CdS/Mo_2C$ are 8002 and 17,472 μmol/(g·h), respectively. The results show that $CdS/MoO_2@Mo_2C$ (CMM5) has much better photocatalytic performance than $CdS/Mo_2C$ and $CdS/MoO_2$. The faster transfer of excited charge carriers and efficient charge separation caused by $MoO_2$ between CdS and $Mo_2C$ MXene can extensively increase the photocatalytic performance of $CdS/Mo_2C$.

## 3.3 Photophysical and photoelectrochemical properties

The light response and photoelectric characters were investigated to understand the photocatalytic processes. Firstly, the UV–Vis diffuse reflectance spectra (DRS) were measured to investigate the photoabsorption behaviors of the photocatalysts. The UV–Vis DRS of the samples are shown in Fig. 6(a). As shown in Fig. 6(a), the light-harvesting capabilities of all CMM*x* samples appeal in the wavelength range of > 520 nm. Moreover, the absorption intensity in the light region ($\lambda$ > 520 nm) increases gradually with the loading of the $MoO_2@Mo_2C$-MXene compound. This is due to the inherent optical property of the $MoO_2@Mo_2C$-MXene compound and the interface between $MoO_2@Mo_2C$-MXene and CdS. The light-harvesting capabilities of the $CdS/Mo_2C$ sample are also shown in Fig. 6(a). This $CdS/Mo_2C$ sample with $Mo_2C$ MXene of 2.5 wt% presented the best $H_2$ production rate of 17,964 μmol/(g·h) among the $CdS/Mo_2C$ samples [43]. As shown in Fig. 6(a), CMM5 has better light-harvesting capability
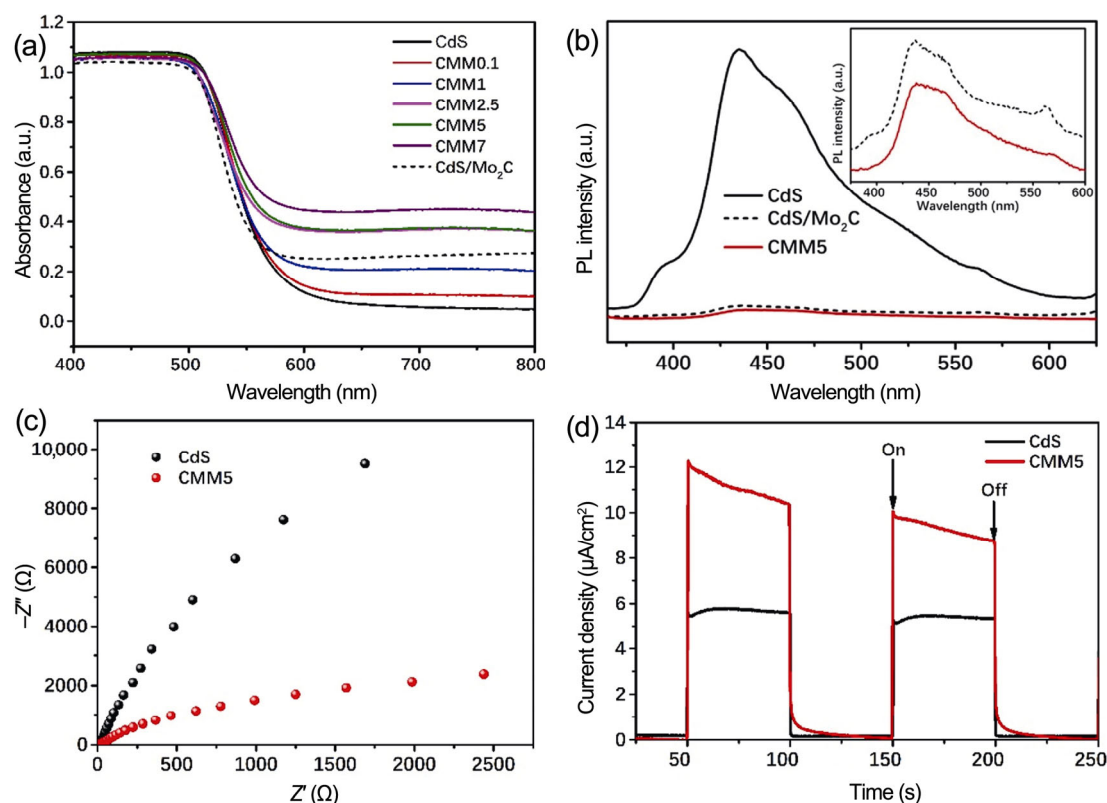


**Fig. 6** (a) UV–Vis DRS of CMM*x* samples and CdS/Mo$_2$C. (b) PL spectra of CdS, CMM5, and CdS/Mo$_2$C. The inset without the CdS spectrum is used to show the PL intensity difference between CMM5 and CdS/Mo$_2$C. (c) EIS plots and (d) TPC responses of CdS and CMM5.

compared to CdS/Mo$_2$C, which corresponds to a better H$_2$ production rate (22,672 μmol/(g·h)). Besides, compared with the pure CdS, the loading of MoO$_2$@Mo$_2$C-MXene makes a gradual absorption edge red-shift and promotes the visible absorption, which is more helpful to promote the progress of the photocatalytic reaction.

The PL spectroscopy was used to analyze the separation efficiencies of photogenerated carriers. The PL spectra of CdS, CMM5, and CdS/Mo$_2$C are shown in Fig. 6(b). The pure CdS exhibits a strong PL peak at 435 nm, indicating the quick photoinduced carrier recombination. In comparison, the PL intensities of CMM5 and CdS/Mo$_2$C decline dramatically, which implies that the photoinduced carrier recombination is effectively suppressed owing to the existence of co-catalyst. Besides, compared with CdS/Mo$_2$C, CMM5 presents the lowest PL intensity, suggesting that CdS/MoO$_2$@Mo$_2$C has a lower electron–hole recombination rate probably due to the "long" reversed flow path of electrons from Mo$_2$C MXene to CdS caused by the MoO$_2$ separation [57].

The charge-transfer efficiency was investigated by the EIS and TPC density measurements, which are shown in Figs. 6(c) and 6(d), respectively. As indicated in Fig. 6(c), CMM5 has a smaller arc radius of charge transfer resistance than CdS, which is indicative of higher separation efficiency of carriers. The TPC responses of CdS and CMM5 were tested by several on–off cycles under illumination. As shown in Fig. 6(d), the photocurrent intensity of CMM5 was significantly higher than that of CdS. This is because the MoO$_2$@Mo$_2$C-MXene composite, as the binary co-catalyst, was effectively to receive photogenerated electrons from CdS. Thus, the photoelectrochemical experiments demonstrate that the introduction of MoO$_2$@Mo$_2$C-MXene can obviously promote the light absorption, charge separation, and transfer.

### 3. 4 Photocatalytic mechanism

The energy band structure of semiconductor samples is crucial to comprehending the mechanism in the photocatalytic system for the H$_2$ evolution activity. The band gap energy ($E_g$) of the samples is calculated by Eq. (1) [58]:

$$(\alpha h v)^{1/n} = A(h v - E_g) \tag{1}$$

where $\alpha$, $h$, $v$, and $A$ are the absorption constant, the Planck constant, the frequency, and the constant,

respectively. Here, the variable $n$ is 1/2 because the nature of CdS is a direct band gap material, and CdS has a characteristic of the n-type semiconductor [59]. Figure 7(a) draws the extrapolated Tauc plots according to Eq. (1) and the corresponding UV–Vis DRS in Fig. 6(a). The $E_g$ of CdS, CMM5, and CdS/Mo$_2$C can hence be estimated at 2.26, 2.23, and 2.25 eV, respectively. Compared with the pure CdS, the $E_g$ of CMM5 and CdS/Mo$_2$C were tuned to be relatively narrow after the loading of MoO$_2$@Mo$_2$C-MXene or Mo$_2$C MXene, resulting in the absorption of the majority of visible light [60].
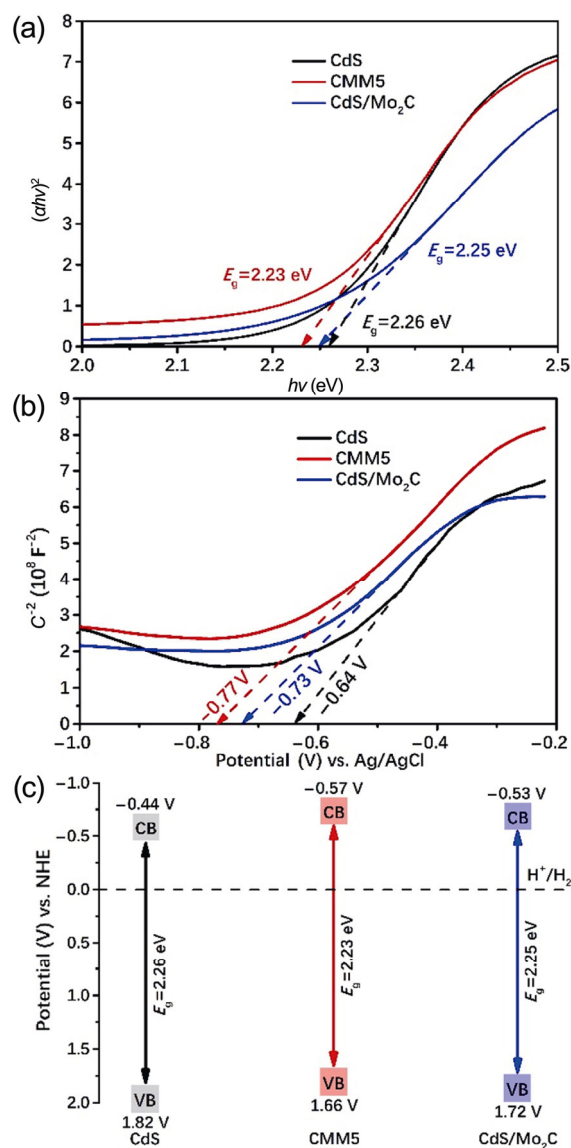


**Fig. 7** (a) Tauc plots and (b) Mott–Schottky plots of CdS, CMM5, and CdS/Mo$_2$C. (c) Schematic illustration of the energy band structures of CdS, CMM5, and CdS/Mo$_2$C.

The positions of conduction band (CB) are determined by the Mott–Schottky plots (Fig. 7(b)). From the Mott–Schottky plots, the flat band potentials ($E_{fb}$) of the photoelectrodes of CdS, CMM5, and CdS/Mo$_2$C can be found to be −0.64, −0.77, and −0.73 V (vs. Ag/AgCl), respectively. Thus, the CB values of CdS, CMM5, and CdS/Mo$_2$C are equivalent to be −0.44, −0.57, and −0.53 V vs. normal hydrogen electrode (NHE), respectively, according to the formula of $E_{NHE}$ = $E_{Ag/AgCl}$ + 0.197 V, because of the little difference between the $E_{fb}$ and the lower CB edge for the n-type semiconductor [61]. According to the $E_g$ values from the Tauc plots in Fig. 6(a) and the calculated CB, the calculated valance band (VB) levels of CdS, CMM5, and CdS/Mo$_2$C are 1.82, 1.66, and 1.72 V vs. NHE, respectively. According to these, the energy band structure can be schematically described in Fig. 7(c). Compared with the pure CdS, CMM5 and CdS/Mo$_2$C have more negative CB levels, while CMM5 exhibits the most negative value of CB. Thus, the photoinduced electrons in the CB region of CdS/MoO$_2$@Mo$_2$C have a stronger reduction capability compared to the case in CdS/Mo$_2$C.

In the n-type semiconductor, the $E_{fb}$ potential is close to the Fermi level ($E_f$) [62]. Therefore, the $E_f$ levels of CdS, CMM5, and CdS/Mo$_2$C can be regarded as −0.44, −0.57, and −0.53 V vs. NHE, respectively. According to the previous works, the $E_f$ values of

MoO$_2$ and Mo$_2$C MXene are calculated to be 0.57 V [63] and 1.09 V [43], respectively. Hence, the electrons migrate from CdS with the electronegative $E_f$ to MoO$_2$@Mo$_2$C-MXene or Mo$_2$C MXene with the electropositive $E_f$ after their combination. Based on the above analysis, the changes in the band structure before and after the combination between CdS and MoO$_2$@Mo$_2$C-MXene or Mo$_2$C MXene are schematically shown in Fig. 8. Before the combination, the $E_f$ of pure CdS is much more negative than those of MoO$_2$ and Mo$_2$C MXene (Figs. 8(a) and 8(d)). After coupling with co-catalysts, the charges are redistributed among them until equilibrium with the reduction of the band gap of CdS (Figs. 8(b) and 8(e)). Thus, their Fermi levels reach the same value [63]. Then, the CB and VB of CdS in CMM5 and CdS/Mo$_2$C are bent "upward". In view of this, a Schottky junction is formed between CdS and co-catalyst due to the remain of positive charges in CdS near the interface, where a space charge layer is formed [64]. Under the visible-light illumination (Figs. 8(c) and 8(f)), CdS is excited to produce electrons and holes. Then the excited photoinduced electrons can be transferred from the VB to the CB in CdS, building up the separation of photoexcited electron–hole pairs. In general, the semiconductor material with a narrow band gap is more beneficial to the solar energy conversion under visible light [60], indicating that it should be possible to irradiate CMM5 with the light of
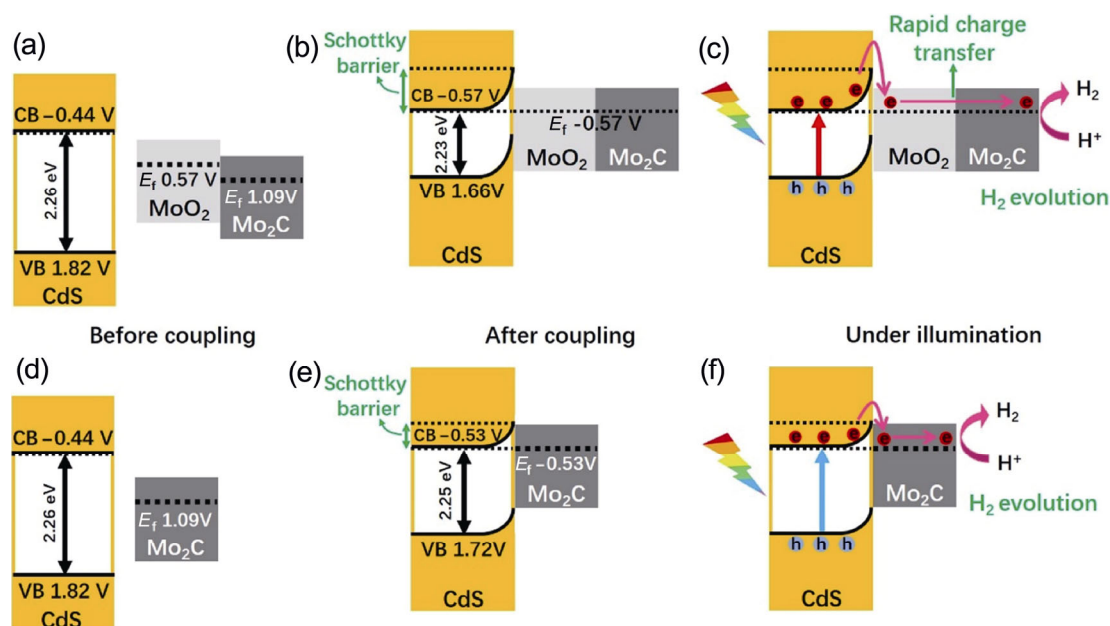


**Fig. 8** Schematic illustration of the changes of the band structures before and after coupling in the case of (a, b) CdS/MoO$_2$@Mo$_2$C and (d, e) CdS/Mo$_2$C. (c, f) Schematic illustration of separation and transfer of photoinduced electrons and holes in the CdS/MoO$_2$@Mo$_2$C and CdS/Mo$_2$C systems under the visible light irradiation.

lower energy than that needed to electronically excite CdS/Mo$_2$C, i.e., the formed separation of photogenerated carriers can be readily achieved for CdS/MoO$_2$@Mo$_2$C in CdS as compared to CdS/Mo$_2$C.

Owing to the restriction of the "upward" bending of the CB and the VB in CdS resulting from the reduced space charge layer thickness [65], the photoinduced electrons in the CB of CdS can still keep going to migrate across the Schottky junction to co-catalyst, leaving the photoinduced holes in the VB of CdS. As a result, the Schottky junction can serve as an electron sink to capture the photoinduced electrons effectively and restrict electrons from diffusing back to CdS. As depicted in Fig. 8, the CB position of CdS becomes more negative, from −0.44 (pure CdS) to −0.57 or −0.53 V vs. NHE after coupling with MoO$_2$@Mo$_2$C-MXene or Mo$_2$C MXene. The more negative CB position in the heterostructure, especially in CdS/MoO$_2$@Mo$_2$C, indicates the formation of a "higher" Schottky junction, which can more effectively prevent electrons from returning to CdS. In view of this, more holes left in the VB can be consumed by the sacrificial reagent, and the further suppressive recombination is achieved.

The contrastive experiments in Fig. S7(a) in the ESM confirm that two CdS samples coupled with MoO$_2$ and Mo$_2$C MXene exhibit lower H$_2$ production capacity than that of CdS/MoO$_2$@Mo$_2$C. Obviously, the formed double heterointerface (CdS–MoO$_2$ and MoO$_2$–Mo$_2$C) plays an important role in the photocatalysis process. After being transferred to the MoO$_2$@Mo$_2$C-MXene composite, the electrons further rapidly shuttle to Mo$_2$C MXene through MoO$_2$.

Both heterointerfaces (CdS–MoO$_2$ and Mo$_2$–Mo$_2$C) are essential for the photocatalysis process. Single CdS–MoO$_2$ heterointerface does not have excellent performance. This is because MoO$_2$ has a high carrier-density. The high carrier-density is often accompanied by a faster recombination rate of photoexcited electron–hole pairs in MoO$_2$ due to the small band gaps [63]. Thus, if there is no Mo$_2$C MXene with a high reduction capability of H$^+$ into H$_2$ as electron trapping, the CdS/MoO$_2$ shows low photocatalytic activity due to the faster recombination rate of photoexcited electron–hole pairs in MoO$_2$. In the CdS/MoO$_2$@Mo$_2$C system, it is more likely that MoO$_2$ should be regarded as an electron-transport bridge for the fast photoinduced electron transferring from CdS to Mo$_2$C MXene due to the existence of the double heterointerface, which is similar with the role of carbon species in some

photocatalytic systems [66–68]. Moreover, in the case of Mo$_2$C MXene being as the single co-catalyst, the migration rate of photoinduced electrons from CdS to Mo$_2$C MXene is "slower" owing to the lack of MoO$_2$ as the electron-transport bridge. The mechanism discussed above and the charge-transfer efficiency are further evidenced by the EIS and TPC in Figs. S7(b) and S7(c) in the ESM, respectively.

Last but not the least, Mo$_2$C MXene has been proved to be an excellent candidate among various MXenes for the photocatalytic H$_2$ production due to its near-zero $\Delta G_{H*}$ and more activity of Mo element. In this case, Mo$_2$C MXene can serve as an electron trapping because of its electropositive $E_f$ position and excellent conductivity. The photoinduced electrons arrive in Mo$_2$C MXene finally and transfer to the active sites on the MXene surface, where the protons in the aqueous solution are efficiently reduced and the reduction of H$^+$ into H$_2$ is achieved by the photoinduced electrons.

Table S3 in the ESM makes a comparison between CdS/MoO$_2$@Mo$_2$C and various state-of-the-art MXene-based and CdS-based photocatalysts previously reported. It is evident that CdS/MoO$_2$@Mo$_2$C made in this paper outperforms most other MXene-based photocatalysts with the best H$_2$ evolution performance, even superior to the noble metal catalysts. Therefore, the novel CdS/MoO$_2$@Mo$_2$C photocatalyst modified based on CdS/Mo$_2$C successfully achieves the further improvement of photocatalytic H$_2$ production and provides new ideas for the application of MXenes in the photocatalysis.

## 4 Conclusions

In summary, the CdS/MoO$_2$@Mo$_2$C photocatalyst was successfully prepared by a two-step hydrothermal method. In this system, CdS grew on the surface of the MoO$_2$@Mo$_2$C-MXene composite and formed an acanthosphere structure. Remarkably, the optimal CdS/MoO$_2$@Mo$_2$C (CMM5) exhibits an ultrahigh H$_2$ production rate of 22,672 μmol/(g·h) under visible light, which is 11.8 times that of CdS. Moreover, the binary co-catalyst of MoO$_2$@Mo$_2$C-MXene based CdS also has higher photocatalytic H$_2$ production activity than that of Mo$_2$C MXene as the single co-catalyst. The experimental results illustrate that CdS/MoO$_2$@Mo$_2$C possesses better photophysical and photoelectrochemical properties compared to CdS/Mo$_2$C due to the presence of MoO$_2$ with excellent electrical conductivity as the

electron-transport bridge between CdS and Mo$_2$C MXene, thereby leading to faster photoinduced electron transfer. The energy band structure reveals that the CB of CdS is tuned to be more negative after coupling with MoO$_2$@Mo$_2$C-MXene compared to the case of CdS/Mo$_2$C, indicating that the resultant "higher" Schottky junction can more effectively restrict electrons from diffusing back to CdS and further achieve the suppressive recombination. Besides, the relatively narrow band gap in CdS/MoO$_2$@Mo$_2$C is beneficial to the visible light absorption. These factors greatly enhance the H$_2$ production of this novel photocatalytic system with the binary co-catalyst as compared to CdS/Mo$_2$C.

## Acknowledgements

## Declaration of competing interest

The authors have no competing interests to declare that are relevant to the content of this article.

## Electronic Supplementary Material

Supplementary material is available in the online version of this article at https://doi.org/10.1007/s40145-022-0621-3.

## References

[1] Li HQ, Wang X, Xu JQ, *et al*. One-dimensional CdS nanostructures: A promising candidate for optoelectronics. *Adv Mater* 2013, **25**: 3017–3037.

[2] Tang ZR, Han B, Han C, *et al*. One dimensional CdS based materials for artificial photoredox reactions. *J Mater Chem A* 2017, **5**: 2387–2410.

[3] Utterback JK, Grennell AN, Wilker MB, *et al*. Observation of trapped-hole diffusion on the surfaces of CdS nanorods. *Nat Chem* 2016, **8**: 1061–1066.

[4] Shen RC, Ren DD, Ding YN, *et al*. Nanostructured CdS for efficient photocatalytic H$_2$ evolution: A review. *Sci China Mater* 2020, **63**: 2153–2188.

[5] Wu KF, Chen ZY, Lv HJ, *et al*. Hole removal rate limits photodriven H$_2$ generation efficiency in CdS–Pt and CdSe/CdS–Pt semiconductor nanorod-metal tip heterostructures. *J Am Chem Soc* 2014, **136**: 7708–7716.

[6] Khon E, Mereshchenko A, Tarnovsky AN, *et al*. Suppression of the plasmon resonance in Au/CdS colloidal nanocomposites. *Nano Lett* 2011, **11**: 1792–1799.

[7] Feng C, Chen ZY, Hou J, *et al*. Effectively enhanced photocatalytic hydrogen production performance of one-pot synthesized MoS$_2$ clusters/CdS nanorod heterojunction material under visible light. *Chem Eng J* 2018, **345**: 404–413.

[8] Li YL, Gao CL, Jiang WS, *et al*. A game-changing design of low-cost, large-size porous cocatalysts decorated by ultra-small photocatalysts for highly efficient hydrogen evolution. *Appl Catal B: Environ* 2021, **286**: 119923.

[9] Tan WY, Li YL, Jiang WS, *et al*. CdS nanospheres decorated with NiS quantum dots as nobel-metal-free photocatalysts for efficient hydrogen evolution. *ACS Appl Energy Mater* 2020, **3**: 8048–8054.

[10] Liang ZZ, Shen RC, Ng YH, *et al*. A review on 2D MoS$_2$ cocatalysts in photocatalytic H$_2$ production. *J Mater Sci Technol* 2020, **56**: 89–121.

[11] Yuan JL, Wen JQ, Gao QZ, *et al*. Amorphous Co$_3$O$_4$ modified CdS nanorods with enhanced visible-light photocatalytic H$_2$-production activity. *Dalton Trans* 2015, **44**: 1680–1689.

[12] Cao J, Sun JZ, Li HY, *et al*. A facile room-temperature chemical reduction method to TiO$_2$@CdS core/sheath heterostructure nanowires. *J Mater Chem* 2004, **14**: 1203–1206.

[13] Peng TY, Li K, Zeng P, *et al*. Enhanced photocatalytic hydrogen production over graphene oxide–cadmium sulfide nanocomposite under visible light irradiation. *J Phys Chem C* 2012, **116**: 22720–22726.

[14] Ran JR, Yu JG, Jaroniec M. Ni(OH)$_2$ modified CdS nanorods for highly efficient visible-light-driven photocatalytic H$_2$ generation. *Green Chem* 2011, **13**: 2708–2713.

[15] Shen RC, Lu XY, Zheng QQ, *et al*. Tracking S-scheme charge transfer pathways in Mo$_2$C/CdS H$_2$-evolution photocatalysts. *Sol RRL* 2021, **5**: 2100177.

[16] Liu FF, Zhou AG, Chen JF, *et al*. Preparation of Ti$_3$C$_2$ and Ti$_2$C MXenes by fluoride salts etching and methane adsorptive properties. *Appl Surf Sci* 2017, **416**: 781–789.

[17] Li ZY, Wang LB, Sun DD, *et al*. Synthesis and thermal stability of two-dimensional carbide MXene Ti$_3$C$_2$. *Mater Sci Eng B* 2015, **191**: 33–40.

[18] Anasori B, Lukatskaya MR, Gogotsi Y. 2D metal carbides and nitrides (MXenes) for energy storage. *Nat Rev Mater* 2017, **2**: 16098.

[19] Zhou AG, Liu Y, Li SB, *et al*. From structural ceramics to 2D materials with multi-applications: A review on the development from MAX phases to MXenes. *J Adv Ceram* 2021, **10**: 1194–1242.

[20] Wu M, He Y, Wang LB, *et al*. Synthesis and electrochemical

properties of V$_2$C MXene by etching in opened/closed environments. *J Adv Ceram* 2020, **9**: 749–758.

[21] Seh ZW, Fredrickson KD, Anasori B, *et al*. Two-dimensional molybdenum carbide (MXene) as an efficient electrocatalyst for hydrogen evolution. *ACS Energy Lett* 2016, **1**: 589–594.

[22] Lei JC, Kutana A, Yakobson BI. Predicting stable phase monolayer Mo$_2$C (MXene), a superconductor with chemically-tunable critical temperature. *J Mater Chem C* 2017, **5**: 3438–3444.

[23] Kim H, Anasori B, Gogotsi Y, *et al*. Thermoelectric properties of two-dimensional molybdenum-based MXenes. *Chem Mater* 2017, **29**: 6472–6479.

[24] Wu M, He M, Hu QK, *et al*. Ti$_3$C$_2$ MXene-based sensors with high selectivity for NH$_3$ detection at room temperature. *ACS Sens* 2019, **4**: 2763–2770.

[25] Guo ZL, Zhou J, Zhu LG, *et al*. MXene: a promising photocatalyst for water splitting. *J Mater Chem A* 2016, **4**: 11446–11452.

[26] Zhang H, Li YL, Li WM, *et al*. Designing large-sized cocatalysts for fast charge separation towards highly efficient visible-light-driven hydrogen evolution. *Int J Hydrogen Energy* 2021, **46**: 28545–28553.

[27] Li WM, Zhuang CQ, Li YL, *et al*. Anchoring ultra-small TiO$_2$ quantum dots onto ultra-thin and large-sized Mxene nanosheets for highly efficient photocatalytic water splitting. *Ceram Int* 2021, **47**: 21769–21776.

[28] Ran JR, Gao GP, Li FT, *et al*. Ti$_3$C$_2$ MXene co-catalyst on metal sulfide photo-absorbers for enhanced visible-light photocatalytic hydrogen production. *Nat Commun* 2017, **8**: 13907.

[29] Bai JX, Shen RC, Chen WL, *et al*. Enhanced photocatalytic H$_2$ evolution based on a Ti$_3$C$_2$/Zn$_{0.7}$Cd$_{0.3}$S/Fe$_2$O$_3$ Ohmic/S-scheme hybrid heterojunction with cascade 2D coupling interfaces. *Chem Eng J* 2022, **429**: 132587.

[30] Bai JX, Shen RC, Jiang ZM, *et al*. Integration of 2D layered CdS/WO$_3$ S-scheme heterojunctions and metallic Ti$_3$C$_2$ MXene-based Ohmic junctions for effective photocatalytic H$_2$ generation. *Chin J Catal* 2022, **43**: 359–369.

[31] Jiang ZM, Chen Q, Zheng QQ, *et al*. Constructing 1D/2D Schottky-based heterojunctions between Mn$_{0.2}$Cd$_{0.8}$S nanorods and Ti$_3$C$_2$ nanosheets for boosted photocatalytic H$_2$ evolution. *Acta Phys Chimi-Sin* 2021, **37**: 2010059.

[32] Yin JJ, Zhan FK, Jiao TF, *et al*. Facile preparation of self-assembled MXene@Au@CdS nanocomposite with enhanced photocatalytic hydrogen production activity. *Sci China Mater* 2020, **63**: 2228–2238.

[33] Li KK, Jiao TF, Xing RR, *et al*. Fabrication of tunable hierarchical MXene@AuNPs nanocomposites constructed by self-reduction reactions with enhanced catalytic performances. *Sci China Mater* 2018, **61**: 728–736.

[34] Huang XX, Wang R, Jiao TF, *et al*. Facile preparation of hierarchical AgNP-loaded MXene/Fe$_3$O$_4$/polymer nanocomposites by electrospinning with enhanced catalytic performance for wastewater treatment. *ACS Omega* 2019, **4**: 1897–1906.

[35] Huang WX, Li ZP, Wu C, *et al*. Delaminating Ti$_3$C$_2$ MXene by blossom of ZnIn$_2$S$_4$ microflowers for noble-metal-free photocatalytic hydrogen production. *J Mater Sci Technol* 2022, **120**: 89–98.

[36] Li ZP, Huang WX, Liu JX, *et al*. Embedding CdS@Au into ultrathin Ti$_{3-x}$C$_2$T$_y$ to build dual Schottky barriers for photocatalytic H$_2$ production. *ACS Catal* 2021, **11**: 8510–8520.

[37] Du H, Zhang QP, Zhao B, *et al*. Novel hierarchical structure of MoS$_2$/TiO$_2$/Ti$_3$C$_2$T$_x$ composites for dramatically enhanced electromagnetic absorbing properties. *J Adv Ceram* 2021, **10**: 1042–1051.

[38] Hu C, Lai CC, Tao Q, *et al*. Mo$_2$Ga$_2$C: A new ternary nanolaminated carbide. *Chem Commun* 2015, **51**: 6560–6563.

[39] Jin S, Su TC, Hu QK, *et al*. Thermal conductivity and electrical transport properties of double-A-layer MAX phase Mo$_2$Ga$_2$C. *Mater Res Lett* 2020, **8**: 158–164.

[40] Jin S, Wang ZT, Du YQ, *et al*. Hot-pressing sintering of double-A-layer MAX phase Mo$_2$Ga$_2$C. *J Inorg Mater* 2020, **35**: 41–45. (in Chinese)

[41] He HT, Jin S, Fan GX, *et al*. Synthesis mechanisms and thermal stability of ternary carbide Mo$_2$Ga$_2$C. *Ceram Int* 2018, **44**: 22289–22296.

[42] Qi XX, Yin WL, Jin S, *et al*. Density-functional-theory predictions of mechanical behaviour and thermal properties as well as experimental hardness of the Ga-bilayer Mo$_2$Ga$_2$C. *J Adv Ceram* 2022, **11**: 273–282.

[43] Jin S, Shi ZH, Jing HJ, *et al*. Mo$_2$C-MXene/CdS heterostructures as visible-light photocatalysts with an ultrahigh hydrogen production rate. *ACS Appl Energy Mater* 2021, **4**: 12754–12766.

[44] Guo YT, Jin S, Wang LB, *et al*. Synthesis of two-dimensional carbide Mo$_2$CT$_x$ MXene by hydrothermal etching with fluorides and its thermal stability. *Ceram Int* 2020, **46**: 19550–19556.

[45] Lang D, Xiang QJ, Qiu GH, *et al*. Effects of crystalline phase and morphology on the visible light photocatalytic H$_2$-production activity of CdS nanocrystals. *Dalton Trans* 2014, **43**: 7245–7253.

[46] Halim J, Kota S, Lukatskaya MR, *et al*. Synthesis and characterization of 2D molybdenum carbide (MXene). *Adv Funct Mater* 2016, **26**: 3118–3127.

[47] Sun YM, Hu XL, Luo W, *et al*. Self-assembled hierarchical MoO$_2$/graphene nanoarchitectures and their application as a high-performance anode material for lithium-ion batteries. *ACS Nano* 2011, **5**: 7100–7107.

[48] Lai CC, Meshkian R, Dahlqvist M, *et al*. Structural and chemical determination of the new nanolaminated carbide Mo$_2$Ga$_2$C from first principles and materials analysis. *Acta Mater* 2015, **99**: 157–164.

[49] Halim J, Cook KM, Naguib M, *et al*. X-ray photoelectron spectroscopy of select multi-layered transition metal carbides (MXenes). *Appl Surf Sci* 2016, **362**: 406–417.

[50] Xie X, Lin L, Liu RY, *et al*. The synergistic effect of metallic molybdenum dioxide nanoparticle decorated

graphene as an active electrocatalyst for an enhanced hydrogen evolution reaction. *J Mater Chem A* 2015, **3**: 8055–8061.

[51] Ovári L, Kiss J, Farkas AP, *et al*. Surface and subsurface oxidation of $Mo_2C/Mo(100)$: Low-energy ion-scattering, auger electron, angle-resolved X-ray photoelectron, and mass spectroscopy studies. *J Phys Chem B* 2005, **109**: 4638–4645.

[52] Benchakar M, Natu V, Elmelegy TA, *et al*. On a two-dimensional $MoS_2/Mo_2CT_x$ hydrogen evolution catalyst obtained by the topotactic sulfurization of $Mo_2CT_x$ MXene. *J Electrochem Soc* 2020, **167**: 124507.

[53] Xu J, Cao XJ. Characterization and mechanism of $MoS_2/CdS$ composite photocatalyst used for hydrogen production from water splitting under visible light. *Chem Eng J* 2015, **260**: 642–648.

[54] Sing KSW. Reporting physisorption data for gas/solid systems with special reference to the determination of surface area and porosity (Recommendations 1984). *Pure Appl Chem* 1985, **57**: 603–619.

[55] Zhou MH, Yu JG, Yu HG. Effects of urea on the microstructure and photocatalytic activity of bimodal mesoporous titania microspheres. *J Mol Catal A Chem* 2009, **313**: 107–113.

[56] Li YJ, Ding L, Yin SJ, *et al*. Photocatalytic $H_2$ evolution on $TiO_2$ assembled with $Ti_3C_2$ MXene and metallic 1T-$WS_2$ as co-catalysts. *Nano Micro Lett* 2020, **12**: 6.

[57] Schvartzman M, Sidorov V, Ritter D, *et al*. Surface passivation of (100) InP by organic thiols and polyimide as characterized by steady-state photoluminescence. *Semicond Sci Tech* 2001, **16**: L68–L71.

[58] Zhang C, Zhou YM, Bao JH, *et al*. Structure regulation of $ZnS@g-C_3N_4/TiO_2$ nanospheres for efficient photocatalytic $H_2$ production under visible-light irradiation. *Chem Eng J* 2018, **346**: 226–237.

[59] Liu J, Liu Y, Liu NY, *et al*. Metal-free efficient photocatalyst for stable visible water splitting via a two-electron pathway. *Science* 2015, **347**: 970–974.

[60] Reza Gholipour M, Dinh CT, Béland F, *et al*. Nanocomposite heterojunctions as sunlight-driven photocatalysts for hydrogen production from water splitting. *Nanoscale* 2015, **7**: 8187–8208.

[61] Li X, Yu JG, Low JX, *et al*. Engineering heterogeneous semiconductors for solar water splitting. *J Mater Chem A* 2015, **3**: 2485–2534.

[62] Zhang Z, Yates JT. Band bending in semiconductors: Chemical and physical consequences at surfaces and interfaces. *Chem Rev* 2012, **112**: 5520–5551.

[63] Hu ZF, Liu G, Chen XQ, *et al*. Enhancing charge separation in metallic photocatalysts: A case study of the conducting molybdenum dioxide. *Adv Funct Mater* 2016, **26**: 4445–4455.

[64] Bai S, Li XY, Kong Q, *et al*. Toward enhanced photocatalytic oxygen evolution: Synergetic utilization of plasmonic effect and Schottky junction via interfacing facet selection. *Adv Mater* 2015, **27**: 3444–3452.

[65] Osterloh FE. Inorganic nanostructures for photoelectrochemical and photocatalytic water splitting. *Chem Soc Rev* 2013, **42**: 2294–2320.

[66] Zhang PY, Song T, Wang TT, *et al*. *In-situ* synthesis of Cu nanoparticles hybridized with carbon quantum dots as a broad spectrum photocatalyst for improvement of photocatalytic $H_2$ evolution. *Appl Catal B: Environ* 2017, **206**: 328–335.

[67] Yuan YJ, Tu JR, Ye ZJ, *et al*. $MoS_2$-graphene/$ZnIn_2S_4$ hierarchical microarchitectures with an electron transport bridge between light-harvesting semiconductor and cocatalyst: A highly efficient photocatalyst for solar hydrogen generation. *Appl Catal B: Environ* 2016, **188**: 13–22.

[68] Xu QL, Cheng B, Yu JG, *et al*. Making co-condensed amorphous carbon/$g-C_3N_4$ composites with improved visible-light photocatalytic $H_2$-production performance using Pt as cocatalyst. *Carbon* 2017, **118**: 241–249.